


Residual fluid flow in liquid metallic droplets processed in the space station electromagnetic levitation facility

Cite as: Phys. Fluids **34**, 077114 (2022); <https://doi.org/10.1063/5.0096768>

Submitted: 21 April 2022 • Accepted: 17 June 2022 • Published Online: 12 July 2022

 Georg Lohöfer and  Xiao Xiao (肖啸)

COLLECTIONS

 This paper was selected as Featured



View Online



Export Citation



CrossMark

ARTICLES YOU MAY BE INTERESTED IN

[Diffusiophoresis of a highly charged conducting fluid droplet](#)

Physics of Fluids **34**, 062013 (2022); <https://doi.org/10.1063/5.0098144>

[The interaction between droplet evaporation and turbulence with interface-resolved direct numerical simulation](#)

Physics of Fluids **34**, 072102 (2022); <https://doi.org/10.1063/5.0096194>

[Interface evolution characteristics of dual droplet successive oblique impact on liquid film](#)

Physics of Fluids **34**, 062115 (2022); <https://doi.org/10.1063/5.0096585>

APL Machine Learning

Open, quality research for the networking communities

Now Open for Submissions

LEARN MORE



Residual fluid flow in liquid metallic droplets processed in the space station electromagnetic levitation facility

Cite as: Phys. Fluids **34**, 077114 (2022); doi: 10.1063/5.0096768

Submitted: 21 April 2022 · Accepted: 17 June 2022 ·

Published Online: 12 July 2022



View Online



Export Citation



CrossMark

Georg Lohöfer^{a)}  and Xiao Xiao (肖啸) 

AFFILIATIONS

Institut für Materialphysik im Weltraum, Deutsches Zentrum für Luft- und Raumfahrt (DLR), 51170 Köln, Germany

^{a)} Author to whom correspondence should be addressed: Georg.Lohoefer@dlr.de

ABSTRACT

The electromagnetic levitation facility on board the International Space Station is used to investigate contactlessly and without gravity-induced convection thermophysical properties and microstructure formations of hot, highly reactive metallic liquids. Despite the widely forceless microgravity environment, the small remaining electromagnetic levitation forces still drive residual convective fluid flows inside the levitated droplet, which may disturb the measurements. Thus, the knowledge of the flow velocities is critical to interpret and evaluate the measurement results. In previous investigations of Xiao and co-workers, a great amount of numerical magneto hydrodynamics calculations were performed with many different material properties and source force terms. The results for the maximum flow velocities hereof were analytically characterized by surrogate models consisting of multi-dimensional, high-order regression analysis. The present work offers another analytical description of these numerical results. Derived based on physical relations, it provides a simpler and physically more illustrative presentation.

© 2022 Author(s). All article content, except where otherwise noted, is licensed under a Creative Commons Attribution (CC BY) license (<http://creativecommons.org/licenses/by/4.0/>). <https://doi.org/10.1063/5.0096768>

I. INTRODUCTION

Electromagnetic levitation is a notably simple and robust technique for the containerless handling of electrically well-conducting liquids.^{1,2} By application of high-frequency alternating magnetic fields, the levitated material of 5–10 mm diameter is heated and melted by the induced eddy currents and stably positioned by the resulting Lorentz forces without external mechanical contact. Together with the use of contactless measurement methods, this enables the investigation of thermophysical properties, such as surface tension, viscosity, electrical resistivity, and density, as well as the investigation of microstructure formations and solidification processes of hot, highly reactive metallic melts or melts in the undercooled liquid state below their melting temperature.^{3–5}

However, all of these measurement methods are more or less severely influenced by the convective and sometimes turbulent fluid flows driven by the electromagnetic levitation forces, which enter (skin effect) the metallic melt.^{6–10} A typical example represents the so-called “oscillating drop method” for the containerless viscosity measurement of a liquid. Its basic idea is to excite surface oscillations on a freely suspended liquid droplet by a short-time pulse of the magnetic levitation

force and to associate their subsequently measured damping, which is due to the viscous shear flow in the droplet, with the viscosity of the liquid via simple physical relations.^{3,11} Obviously, this method delivers reasonable results only if the fluid flow in the droplet originating from the oscillations is only weakly distorted by the convective fluid flow driven by the magnetic levitation forces.

On the ground, the levitation forces, necessary to lift a metallic droplet of 5–8 mm diameter against its weight, generate convective fluid flows in the liquid of a strength that renders a reasonable application of the oscillating drop method impossible. This is, however, different if electromagnetic levitation and viscosity measurement are performed under “microgravity” (μg) conditions in the “ISS-EML” electromagnetic levitation facility on board the “International Space Station.” In this case, the task of the high-frequency magnetic levitation fields consists alone in the containerless confinement of the metallic droplet at a predefined location against external residual forces and in its inductive heating and melting.

The ISS-EML facility^{12–14} uses two superposed high-frequency magnetic fields $\mathbf{B}_E(t) = \mathbf{B}_{E,0} \sin(\omega t)$, as sketched in Fig. 1. A symmetric quadrupole type “positioning field” produced by two

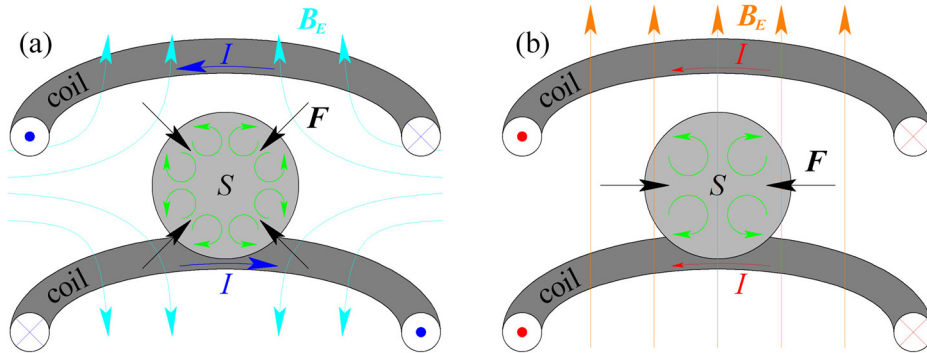


FIG. 1. Sketch of a spherical sample S in the center of circular coil windings. The external high-frequency magnetic quadrupole (a) and dipole (b) fields B_E generated by the respective coil currents I are used for the containerless positioning and heating of S in μg , respectively. Outlined are also the magnetic Lorentz forces F (black arrows) in S , resulting from the respective B_E -field, and the characteristic pattern of the driven fluid flow (green arrows) in the liquid sample.

equal, parallel, and coaxial circular rf currents (≈ 150 kHz) of the same strength but opposite directions, the resulting total force $F \propto -\mathbf{B}_{E,0} \cdot \nabla \mathbf{B}_{E,0}$ of which repels a displaced weightless metallic droplet to its center between the two coils where the field strength is weakest, as shown in Fig. 1(a). Additionally, a widely homogeneous dipole type “heating field,” generated by two parallel and coaxial circular rf currents (≈ 370 kHz) of the same strength and in the same directions, the total induced heating power $P \propto \mathbf{B}_{E,0}^2$ of which enables an efficient heating of the metal specimen, as shown in Fig. 1(b).

The typical experiment run in the μg ISS-EML facility (for details, see, e.g., Ref. 14) consists essentially of two phases:

1. The “heating phase,” where the originally solid metal sample, positioned in the center of the coils by a strong magnetic positioning field, is heated, melted, and overheated a few hundred Kelvin over its melting temperature by a strong magnetic heating field.
2. The subsequent and primarily interesting cooling or “experimental phase,” where the magnetic heating field is reduced to its technically lowest possible value, and where the magnetic positioning field is reduced to a value that still keeps the droplet safely in place against possible external residual accelerations. In this phase, the experiments on the droplets take place, after the strong disturbances in the liquid from the heating phase decayed within the first few seconds.⁸

As video images show,¹⁴ the deformation of the levitated droplets from the spherical shape is during the experimental phase typically in the range of 0.5% only and thus negligible. This is due to the fact that during this phase, the surface tension of the small metal droplets is much higher than the distorting surface pressure from the low remaining magnetic forces. Furthermore, there are generally no fluctuations on the free surface visible during this phase indicating a laminar or at most a weak turbulent fluid flow near the boundary.

Nevertheless, the remaining magnetic forces in the experimental phase still drive a steady “residual fluid flow” in the droplet (see the example in Sec. V A), which, depending on its strength, may non-negligibly interfere with the flow resulting from the oscillating drop method. This becomes evident when viscosity measurements, especially performed on low viscous liquid droplets, by the oscillating drop method provide physically meaningless values.¹⁵ Thus, it is necessary for the experiment preparation to predict the strength of this steady residual fluid flow inside the levitated droplet in terms of the sample and facility parameters. In the following, we investigate this flow in an

undisturbed spherical liquid droplet placed in the high-frequency magnetic fields of the micro-g ISS-EML levitation facility. A first attempt to calculate residual flow velocities driven by the magnetic levitation forces from a purely analytical approach has already been performed by Li,¹⁶ however, under restricting conditions.

II. THE SURROGATE MODEL OF Xiao *et al.*

A more useful analytical description is available by the surrogate modeling of Xiao *et al.*^{17,18} They performed numerical magneto hydrodynamics (MHD) simulations for a spherical, electrically conducting, liquid droplet of 6.5 mm in diameter located in the center of either a rf magnetic dipole or quadrupole field, which approximates the equivalent heating or positioning field of the ISS-EML electromagnetic levitation facility, cf. Fig. 1. These calculations were performed for a great amount of different values of the sample properties: density ρ , viscosity η , and electrical conductivity σ , covering ranges $5 \text{ g/cm}^3 \leq \rho \leq 10 \text{ g/cm}^3$, $1 \times 10^{-3} \text{ Pa s} \leq \eta \leq 40 \times 10^{-3} \text{ Pa s}$, and $0.5 \times 10^6 (\Omega\text{m})^{-1} \leq \sigma \leq 5 \times 10^6 (\Omega\text{m})^{-1}$, which are typical for the most liquid metallic alloys, and for various magnetic field strengths, the generating coil current of which is externally predetermined by a facility control voltage U_{ctr} . Depending on the Reynolds number, Re , in the resulting fluid flows, these numerical calculations were performed either with the use of a laminar code, for $Re \lesssim 300$, or with the use of a turbulent Renormalization Group (RNG) $k-\epsilon$ code for $Re \gtrsim 300$. The typical patterns of the internal convective fluid flow fields are shown in Fig. 2.

The maximum flow velocities u_{max} in the liquid sample as function of the different sample and facility parameters ($\rho, \eta, \sigma, U_{ctr}$) were analytically presented by the authors by means of a four-dimensional polynomial (the surrogate model)

$$u_{max}(\rho, \eta, \sigma, U_{ctr}) = \sum_{i,j,k,s} p_{i,j,k,s} U_{ctr}^i \rho^j \ln(\eta)^k \ln(\sigma)^s \quad (1)$$

with coefficients $p_{i,j,k,s}$, which were fitted to the corresponding numerical results for u_{max} . It turns out that at least a third-order fit with up to 21 parameters has to be performed for a reasonable match.

III. THE PHYSICAL MODEL

Compared with the surrogate model of Eq. (1), the analytical expression for u_{max} as function of ($\rho, \eta, \sigma, U_{ctr}$) can considerably be reduced when physical relations between the occurring quantities are considered. On this basis, an analytical formula is derived in this

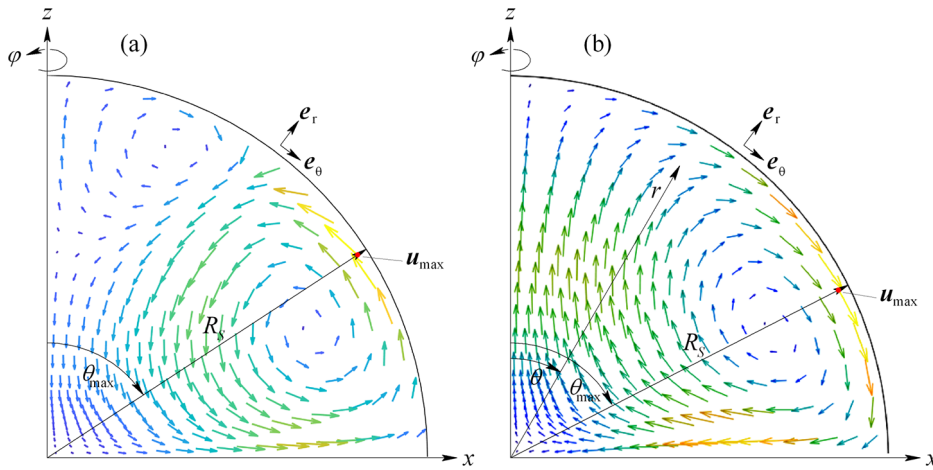


FIG. 2. Examples for the characteristic axially- and mirror-symmetric fluid flow patterns inside the upper section of a liquid electrically conducting sphere processed in the ISS-EML levitation facility. The flow in (a) is driven by the facility's rf magnetic positioning field and that one in (b) by its rf magnetic heating field, cf. Fig. 1. The red dots indicate the locations of the maximum flow velocity, which occur on the boundary of the sphere. The diagrams result from the numerical MHD calculations of Xiao *et al.*¹⁸

section containing only three *a priori* unknown coefficients. These are determined in Sec. IV by a multilinear fit (regression analysis) of the analytical formula to the great amount of numerical MHD results of Xiao *et al.*,¹⁸ see above.

A. Basics

Just as for the above-mentioned numerical simulations, the basis for the following physical analytic model are the classical non-linear MHD equations applied on an incompressible liquid spherical drop $S := \{\mathbf{x} \in \mathbb{R}^3 : \|\mathbf{x}\| < R_S\}$ of radius R_S . Due to the weak Lorentz forces in the microgravity environment, the assumption of a spherical shape represents a reasonable simplification. Due to the constant mass density ρ , the steady flow field $\mathbf{u}(\mathbf{x})$ in S can well be described by the mass conservation equation

$$\nabla \cdot \mathbf{u}(\mathbf{x}) = 0 \quad (2)$$

and the steady incompressible Navier–Stokes momentum conservation equation

$$\rho \mathbf{u}(\mathbf{x}) \cdot \nabla \mathbf{u}(\mathbf{x}) = -\nabla p(\mathbf{x}) + \eta \Delta \mathbf{u}(\mathbf{x}) + \mathbf{f}(\mathbf{x}). \quad (3)$$

The terms on the right-hand side of Eq. (3) describe the internal stress on a liquid volume element resulting from the pressure $p(\mathbf{x})$, the viscous shear flow with constant coefficient η , and the external electromagnetic Lorentz force density $\mathbf{f}(\mathbf{x})$. The appropriate conditions at the boundary points \mathbf{x}_B between the liquid droplet and a surrounding vacuum are determined on the one hand from the conservation of mass flow at the free boundary surface

$$\mathbf{n}(\mathbf{x}_B) \cdot \mathbf{u}(\mathbf{x}_B) = 0, \quad (4)$$

meaning that there is no flux in the normal direction $\mathbf{n}(\mathbf{x}_B)$ on the free surface and, on the other hand, from the conservation of momentum in tangential direction $\boldsymbol{\tau}(\mathbf{x}_B)$ at the free boundary surface

$$\mathbf{n}(\mathbf{x}_B) \cdot \left(\nabla \mathbf{u}(\mathbf{x})|_{\mathbf{x}=\mathbf{x}_B} + [\nabla \mathbf{u}(\mathbf{x})]^T|_{\mathbf{x}=\mathbf{x}_B} \right) \cdot \boldsymbol{\tau}(\mathbf{x}_B) = 0, \quad (5)$$

meaning that there is no shear stress on the fluid flow from outside of the sample.

As shown in Sec. III C, the rotational invariant geometry of the sample and coil system, outlined in Fig. 1, is transferred to the

symmetry of the external electromagnetic force field $\mathbf{f}(\mathbf{x})$ and to the steady fluid flow field $\mathbf{u}(\mathbf{x})$ in S . This means that $\mathbf{f}(\mathbf{x})$ and analogously $\mathbf{u}(\mathbf{x})$ are two-dimensional only and that the basic Navier–Stokes equation (3) is a two-component vector equation in the (r, θ) half-plane. The solenoidal flow patterns revealed by Fig. 2 suggest to apply the curl operator $\nabla \times$ on Eq. (3). This cancels the pressure term $\nabla p(\mathbf{x})$ but, according to Sec. III C, not the non-conservative external force term $\mathbf{f}(\mathbf{x})$. Using the vector identities $\mathbf{u} \times (\nabla \times \mathbf{u}) \equiv \nabla[\mathbf{u} \cdot \mathbf{u}]/2 - \mathbf{u} \cdot \nabla \mathbf{u}$ and $\nabla \times [\nabla \times \boldsymbol{\Omega}] \equiv \nabla \nabla \cdot \boldsymbol{\Omega} - \Delta \boldsymbol{\Omega}$, the modified Navier–Stokes equation then reads

$$\rho \nabla \times [\mathbf{u}(\mathbf{x}) \times \boldsymbol{\Omega}(\mathbf{x})] - \eta \nabla \times [\nabla \times \boldsymbol{\Omega}(\mathbf{x})] + \nabla \times \mathbf{f}(\mathbf{x}) = \mathbf{0} \quad (6)$$

after the vorticity

$$\boldsymbol{\Omega}(\mathbf{x}) := \nabla \times \mathbf{u}(\mathbf{x}) \quad (7)$$

has been introduced. Since the curl operator points in a direction perpendicular to the direction of its operand and perpendicular to the gradient of its magnitude, it is not difficult to recognize that the three terms in (6) point all in the same direction $\mathbf{e}_r \times \mathbf{e}_\theta = \mathbf{e}_\varphi$ perpendicular to the (r, θ) half-plane, cf. Fig. 2, which reduces (6) to a single scalar equation. To obtain the appropriate condition of (6) at the boundary points \mathbf{x}_B between the liquid droplet and the surrounding vacuum, let us assume that the fluid parameters (ρ, η, σ) drop in a tiny neighborhood around the boundary of S smoothly from its non-zero constant value inside of S to its zero value outside of S . Then, the application of the well-known “pillbox” procedure, cf. for example, (Ref. 19, Appendix A), on the compressible Navier–Stokes equation in this area results finally in the constraint

$$-\rho \mathbf{n}(\mathbf{x}_B) \times \left(\mathbf{u}(\mathbf{x}_B) \cdot \nabla \mathbf{u}(\mathbf{x})|_{\mathbf{x}=\mathbf{x}_B} \right) - \eta \mathbf{n}(\mathbf{x}_B) \times (\nabla \times \boldsymbol{\Omega}(\mathbf{x})|_{\mathbf{x}=\mathbf{x}_B}) + \mathbf{n}(\mathbf{x}_B) \times \mathbf{f}(\mathbf{x}_B) = \mathbf{0}. \quad (8)$$

As for the surrogate model, we are interested for our physical model in the value of the maximum velocity $u_{\max} := \max\|\mathbf{u}(\mathbf{x})\|$ of the flow field in S . Due to the slip flow condition (5) at the free outer boundary of S , and since also the flow driving force $\mathbf{f}(\mathbf{x})$ is maximal there (skin effect), see Sec. III C4, we expect u_{\max} to occur on the boundary $\|\mathbf{x}\| = R_S$ of S what is also confirmed by the numerical MHD calculations, see the examples of Fig. 2. This means that we are

mainly interested in the behavior of the flow field $\mathbf{u}(\mathbf{x})$ in the neighborhood of the boundary. In this respect, the three terms of Eq. (6) are investigated in detail in the following.

B. Turbulence

As mentioned in Sec. II, Xiao *et al.*¹⁸ applied for the numerical calculation of the mean velocity field $\bar{\mathbf{u}}(\mathbf{x})$ of a turbulent fluid flow in S an appropriate RNG $k-\epsilon$ code. In order to model also those results analytically, the turbulent flow velocity field

$$\mathbf{u}(\mathbf{x}) = \bar{\mathbf{u}}(\mathbf{x}) + \mathbf{u}'(\mathbf{x})$$

is generally split in the mean field $\bar{\mathbf{u}}(\mathbf{x})$ and a fluctuating remainder $\mathbf{u}'(\mathbf{x})$. Similar to the laminar case, we look here only for a physical model of the maximal mean velocity $\bar{u}_{\max} := \max\|\bar{\mathbf{u}}(\mathbf{x})\| = \|\bar{\mathbf{u}}(\mathbf{x}_{\max})\|$ of the turbulent flow field, the location \mathbf{x}_{\max} of which is assumed by the same reasons as before to occur on the free boundary $\|\mathbf{x}_{\max}\| = R_S$ of S .

Since, as mentioned above, a fluctuation or jitter of the spherically shaped, free surface is during the experimental phase generally not observed, we expect that the magnitude of the remainder $\mathbf{u}' := \|\mathbf{u}'(\mathbf{x}_{\max})\|$ is on the boundary of S only a small quantity $u' \ll \bar{u}_{\max}$ compared to \bar{u}_{\max} . Thus, we neglect in the following the fluctuating remainder term $\mathbf{u}'(\mathbf{x})$ in our calculations for the maximal mean flow velocity \bar{u}_{\max} in the neighborhood of the boundary. As a consequence of this, the analytical calculations for the turbulent case will structurally be the same as those for the laminar case except that $\mathbf{u}(\mathbf{x})$ and u_{\max} are replaced by $\bar{\mathbf{u}}(\mathbf{x})$ and \bar{u}_{\max} , respectively. The justification of this assumption will turn out when the results of the analytical model are compared with the data from the numerical RNG $k-\epsilon$ model in Sec. IV.

C. The local electromagnetic force density fields

When an electrically conducting sample, in the present case a liquid metallic sphere $S := \{\mathbf{x} \in \mathbb{R}^3 : \|\mathbf{x}\| < R_S\}$ of radius R_S , is placed in an alternating magnetic field $\mathbf{B}(\mathbf{x}, t) = \mathbf{B}_0(\mathbf{x}) \cos(\omega t + \phi) = \text{Re}[\tilde{\mathbf{B}}(\mathbf{x})e^{i\omega t}]$ of angular frequency ω , the induced electric field $\mathbf{E}(\mathbf{x}, t) = \text{Re}[\tilde{\mathbf{E}}(\mathbf{x})e^{i\omega t}]$ drives an alternating current density field $\mathbf{j}_S(\mathbf{x}, t) = \text{Re}[\tilde{\mathbf{j}}_S(\mathbf{x})e^{i\omega t}]$ in S . (In the following, complex-valued quantities are marked by a tilde \sim and their complex conjugated counterparts additionally by the superscript $*$.) In consideration of Ohm's law in moving media (Ref. 20, Sec. 10.2) and Faraday's induction law (Ref. 20, Sec. 6.1), a relation between $\tilde{\mathbf{B}}(\mathbf{x})$ and $\tilde{\mathbf{j}}_S(\mathbf{x})$ reads for $\mathbf{x} \in S$

$$\nabla \times \tilde{\mathbf{j}}_S(\mathbf{x}) = \sigma(-i\omega\tilde{\mathbf{B}}(\mathbf{x}) + \nabla \times [\mathbf{u}(\mathbf{x}) \times \tilde{\mathbf{B}}(\mathbf{x})]) \approx -i\omega\sigma\tilde{\mathbf{B}}(\mathbf{x}), \quad (9)$$

where σ denotes the constant electrical conductivity in S . In the present case, the frequencies $\omega/2\pi > 150$ kHz, the flow velocities $\|\mathbf{u}\| < 1$ m/s (Ref. 18), and the occurring characteristic length scales $L \geq \delta > 0.1$ mm in S , where δ is the skin depth defined in Eq. (20), result in very small magnetic Reynolds numbers $Rm := \|\mathbf{u}\|/(\omega L) < 0.01$, which justifies the neglect of the fluid flow dependent term in (9). In the following, the steady local force density $\mathbf{f}(\mathbf{x})$ for points $\mathbf{x} \in S$ is defined as the time average of the alternating Lorentz force density, that is, $\mathbf{f}(\mathbf{x}) := \overline{\tilde{\mathbf{j}}_S(\mathbf{x}, t) \times \mathbf{B}(\mathbf{x}, t)}$. In complex notation, this reads

$$\mathbf{f}(\mathbf{x}) = \frac{1}{2} \text{Re}[\tilde{\mathbf{j}}_S(\mathbf{x}) \times \tilde{\mathbf{B}}^*(\mathbf{x})] = \frac{1}{2\omega\sigma} \text{Im}[\tilde{\mathbf{j}}_S(\mathbf{x}) \times (\nabla \times \tilde{\mathbf{j}}_S^*(\mathbf{x}))], \quad (10)$$

where the last expression results from (9).

1. Induced current density field

In the steady state, the alternating magnetic field $\mathbf{B}(\mathbf{x}, t)$ and, according to (9), also the alternating current density field $\mathbf{j}_S(\mathbf{x}, t)$ induced in the spherical sample S are maintained by an external alternating current density distribution $\mathbf{j}_E(\mathbf{x}, t) = \text{Re}[\tilde{\mathbf{j}}_E(\mathbf{x})e^{i\omega t}]$ in the coils $\|\mathbf{x}\| \geq R_E$ surrounding S as indicated in Fig. 1. In [Ref. 19, Eq. (3.26)] $\tilde{\mathbf{j}}_S(\mathbf{x})$, $\mathbf{x} \in S$ has been derived for arbitrary three-dimensional external current densities $\tilde{\mathbf{j}}_E(\mathbf{x})$, $\|\mathbf{x}\| \geq R_E$ in terms of an expansion in spherical harmonics. In the present case, the whole system of spherical sample S and surrounding coils is rotationally invariant around the z axis. In spherical coordinates, $\mathbf{x} = (r, \theta, \varphi)$ with origin in the center of S , see Fig. 3, and orthogonal spherical unit vectors $\mathbf{e}_r(\theta, \varphi)$, $\mathbf{e}_\theta(\theta, \varphi)$, and $\mathbf{e}_\varphi(\varphi)$ defined in Eq. (A1), this means that the external current density distribution

$$\tilde{\mathbf{j}}_E(r, \theta, \varphi) = \tilde{j}_E(r, \theta) \mathbf{e}_\varphi(\varphi) \quad (11)$$

confined to the coils in the area $r \geq R_E$, flows in φ -direction only, and has a magnitude $\tilde{j}_E(r, \theta)$, which is independent of the φ -coordinate. Under these conditions, $\tilde{\mathbf{j}}_S(\mathbf{x})$ of [Ref. 19, Eq. (3.26)] simplifies for $r \leq R_S$ likewise to

$$\tilde{\mathbf{j}}_S(r, \theta, \varphi) = \tilde{j}_S(r, \theta) \mathbf{e}_\varphi(\varphi) \quad (12)$$

with

$$\tilde{j}_S(r, \theta) = \frac{\tilde{I}_E}{2R_S^2} \sum_{l=1}^{\infty} R_S^l C_l [\tilde{j}_E] P_l^1(\cos \theta) \tilde{\Gamma}_l(r), \quad (13)$$

where \tilde{I}_E is the (complex) total current through each coil winding and $P_l^1(\cos \theta)$ the first-order associated Legendre function of degree l ,

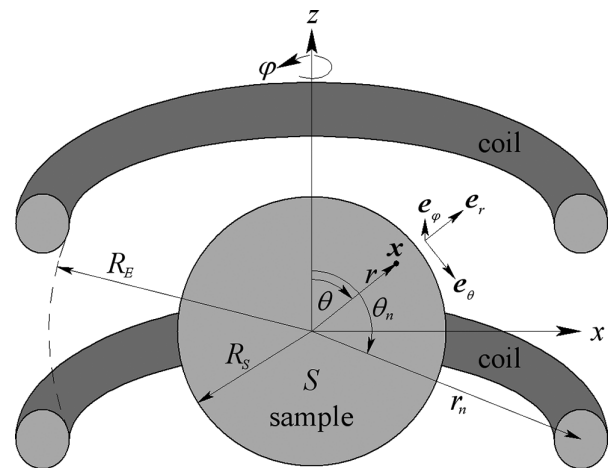


FIG. 3. Sketch of the geometrical arrangement of spherical sample S and surrounding coil windings together with the applied coordinates, unit vectors, and dimensions.

which determines the functional dependence of $\tilde{j}_S(r, \theta)$ on the polar angle θ .

The real valued coefficient

$$C_l[\tilde{j}_E] := \frac{2l+1}{l(l+1)} \int_{R_E}^{\infty} \int_0^{\pi} \frac{\tilde{j}_E(r', \theta')}{\tilde{I}_E} r'^{-l+1} P_l^1(\cos \theta') \sin \theta' d\theta' dr' \quad (14)$$

describes the influence of the external current density distribution $\tilde{j}_E(r, \theta)$ on $\tilde{j}_S(r, \theta)$ and simplifies itself for the idealized case of N thin circular current loops of coordinates (r_n, θ_n) and current directions $\text{sig}_n = +1, -1$, see Fig. 3 and (Ref. 2, Sec. 5), to

$$C_l(r_n, \theta_n) = \frac{2l+1}{l(l+1)} \sum_{n=1}^N \text{sig}_n r_n^{-l} \sin \theta_n P_l^1(\cos \theta_n). \quad (15)$$

For a mirror-symmetric external current density distribution relative to the (x, y) plane through the center of S with $\tilde{j}_E(r, \theta) = \tilde{j}_E(r, \pi - \theta)$, which causes the dipole type magnetic heating field of the EML levitation facility sketched in Fig. 1(b), Eq. (14) implies, due to the property: $P_l^1(-\cos \theta) = (-1)^{l+1} P_l^1(\cos \theta)$, that

$$C_l[\tilde{j}_E(r, \theta) = \tilde{j}_E(r, \pi - \theta)] \neq 0 \quad \text{only if } l = 1, 3, 5, \dots \quad (16)$$

Similarly, for an inverted mirror symmetric external current density distributions with $\tilde{j}_E(r, \theta) = -\tilde{j}_E(r, \pi - \theta)$, which causes the quadrupole type magnetic positioning field of the EML levitation facility sketched in Fig. 1(a), Eq. (14) implies that

$$C_l[\tilde{j}_E(r, \theta) = -\tilde{j}_E(r, \pi - \theta)] \neq 0 \quad \text{only if } l = 2, 4, 6, \dots \quad (17)$$

According to Eq. (14) or (15), the magnitude of the single terms in the expansion of (13) behaves as $R_S^l C_l[\tilde{j}_E] = O((R_S/R_E)^l)$. The magnet coils of the ISS-EML levitation facility are designed such that already the lowest order term of the expansion (13) alone, that is,

$$\tilde{j}_S(r, \theta) = \frac{\tilde{I}_E}{2R_S^2} R_S^l C_l[\tilde{j}_E] P_l^1(\cos \theta) \tilde{\Gamma}_l(r), \quad (18)$$

approximates very well for $l=1$ the current density distribution induced in the spherical sample S by the external magnetic heating field, and for $l=2$, the current density distribution induced in S by the external magnetic positioning field.

The dependence of $\tilde{j}_S(r, \theta)$ on the radial r -coordinate is determined by the complex function

$$\tilde{\Gamma}_l(r) := \frac{\tilde{z}}{\sqrt{r/R_S}} \frac{J_{l+1/2}(\tilde{z}r/R_S)}{J_{l-1/2}(\tilde{z})}, \quad (19)$$

where $J_{l+1/2}$ denotes the half-integer order Bessel functions. $\tilde{\Gamma}_l(r)$ depends via

$$\tilde{z} := (1-i)q, \quad q := R_S/\delta, \quad \text{and} \quad \delta := \sqrt{2/(\mu_0 \omega \sigma)} \quad (20)$$

on the skin depth δ and thus on the electrical conductivity σ of the material in S and on the angular frequency ω of the respective magnetic field. In Eq. (20), μ_0 denotes the magnetic vacuum permeability.

2. Force density in rotationally invariant systems

For rotationally invariant current density distributions $\tilde{j}_S(\mathbf{x}) = \tilde{j}_S(r, \theta) \mathbf{e}_\varphi(\varphi)$, as in the present case, the force density, defined in Eq. (10) for $r \leq R_S$, amounts to

$$\begin{aligned} \mathbf{f}(\mathbf{x}) &= \frac{1}{2\omega\sigma} \text{Im} \left[\tilde{j}_S(r, \theta)^2 \mathbf{e}_\varphi \times (\nabla \times \mathbf{e}_\varphi) \right. \\ &\quad \left. + \tilde{j}_S(r, \theta) \mathbf{e}_\varphi \times \left(\nabla \left[\tilde{j}_S^*(r, \theta) \right] \times \mathbf{e}_\varphi \right) \right] \\ &= \frac{1}{2\omega\sigma} \text{Im} \left[\tilde{j}_S(r, \theta) \nabla \left[\tilde{j}_S^*(r, \theta) \right] \mathbf{e}_\varphi \cdot \mathbf{e}_\varphi - \tilde{j}_S(r, \theta) \mathbf{e}_\varphi \cdot \nabla \tilde{j}_S^*(r, \theta) \right] \\ &= \frac{1}{2\omega\sigma} \text{Im} \left[\tilde{j}_S(r, \theta) \nabla \tilde{j}_S^*(r, \theta) \right], \end{aligned} \quad (21)$$

where the second term results from the application of the well-known double vector product rule. (Here and in the following the operand of a differential operator is set in brackets in cases of doubt.) With the definitions in Eq. (20) and with the explicit representation of the gradient ∇ in spherical coordinates (A2), the local electromagnetic force density (21) in S simplifies for the special case of a rotationally invariant system of sample and coil around the z axis to

$$\mathbf{f}(r, \theta) = \frac{\mu_0}{4} \delta^2 \text{Im} \left[\mathbf{e}_r \tilde{j}_S(r, \theta) \frac{\partial}{\partial r} \tilde{j}_S^*(r, \theta) + \mathbf{e}_\theta \tilde{j}_S(r, \theta) \frac{1}{r} \frac{\partial}{\partial \theta} \tilde{j}_S^*(r, \theta) \right]. \quad (22)$$

Application of the curl operator on \mathbf{f} finally yields

$$\begin{aligned} \nabla \times \mathbf{f}(r, \theta) &= \frac{\mu_0}{4} \delta^2 \text{Im} \left[\nabla \tilde{j}_S(r, \theta) \times \nabla \tilde{j}_S^*(r, \theta) \right] \\ &= \mathbf{e}_\varphi \frac{\mu_0}{2} \delta^2 \text{Im} \left[\frac{\partial}{\partial r} \tilde{j}_S(r, \theta) \frac{1}{r} \frac{\partial}{\partial \theta} \tilde{j}_S^*(r, \theta) \right]. \end{aligned} \quad (23)$$

3. Force densities of the EML heating and positioning fields

Insertion of $\tilde{j}_S(r, \theta)$ from (18) in Eq. (22) yields the local force densities

$$\begin{aligned} \mathbf{f}_l(\mathbf{x}) &= -\mathbf{e}_r(\theta, \varphi) \frac{\mu_0}{8} \frac{|\tilde{I}_E|^2}{R_S^3} \left(R_S^l C_l[\tilde{j}_E] \right)^2 \left(P_l^1(\cos \theta) \right)^2 \\ &\quad \times \frac{R_S}{2q^2} \text{Im} \left[\tilde{\Gamma}_l^*(r) \frac{\partial}{\partial r} \tilde{\Gamma}_l(r) \right] \end{aligned} \quad (24)$$

exerted on points $\mathbf{x} \in S$ either by the magnetic heating field, if $l=1$, or by the magnetic positioning field, if $l=2$, of the ISS-EML facility. In Eq. (24), $|\tilde{I}_E|$ is just the amplitude of the total alternating coil current. Due to $P_1^1(\cos \theta) = \sin \theta$ and $P_2^1(\cos \theta) = 3 \sin \theta \cos \theta$, the maximum local force of the heating field occurs at $\theta = \pi/2$ and that one of the positioning field at $\theta = \pi/4$ and $\theta = 3\pi/4$, respectively, as already sketched in Fig. 1 and plotted in Fig. 4. Insertion of $\tilde{j}_S(r, \theta)$ in Eq. (23) yields analogously

$$\begin{aligned} \nabla \times \mathbf{f}_l(\mathbf{x}) &= \mathbf{e}_\varphi(\varphi) \frac{\mu_0}{8} \frac{|\tilde{I}_E|^2}{R_S^3} \left(R_S^l C_l[\tilde{j}_E] \right)^2 \frac{\partial}{\partial \theta} \left(P_l^1(\cos \theta) \right)^2 \\ &\quad \times \frac{R_S}{r} \frac{R_S}{2q^2} \text{Im} \left[\tilde{\Gamma}_l^*(r) \frac{\partial}{\partial r} \tilde{\Gamma}_l(r) \right]. \end{aligned} \quad (25)$$

With the definition of $\tilde{\Gamma}_l(r)$ in Eq. (19) and in consideration of the recurrence relation of the Bessel functions [Ref. 21, Eq. (9.1.27)], the differentiation of $\tilde{\Gamma}_l(r)$ yields with the definition of $\tilde{z} := (1-i)q$,

$$R_S \frac{\partial}{\partial r} \tilde{\Gamma}_l(r) = \frac{\tilde{z} (\tilde{z}r/R_S J_{l-1/2}(\tilde{z}r/R_S) - (l+1) J_{l+1/2}(\tilde{z}r/R_S))}{(r/R_S)^{3/2} J_{l-1/2}(\tilde{z})}$$

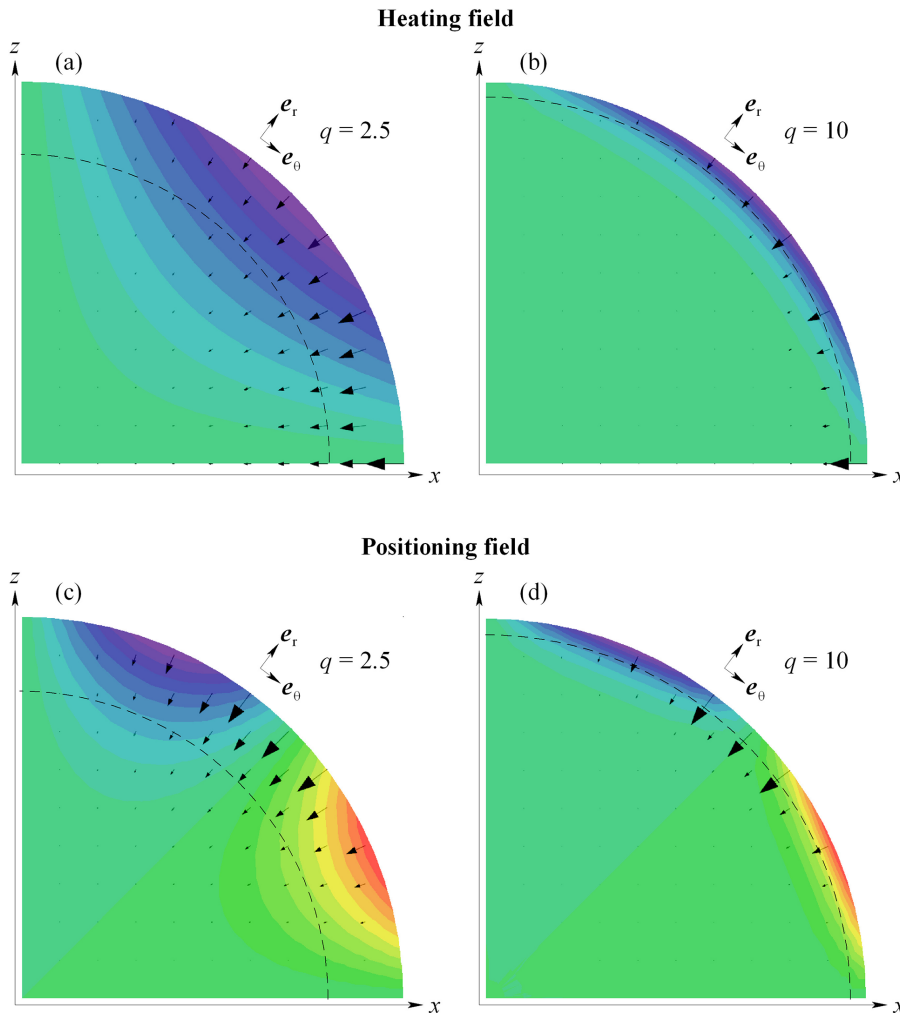


FIG. 4. Diagrams showing superposed the behavior of the electromagnetic heating ((a) and (b)) and positioning ((c) and (d)) force density field $\mathbf{f}(\mathbf{x})$ (vector diagram) and its curl $\nabla \times \mathbf{f}(\mathbf{x})$ (contour map) for two different values of q inside of the upper section of S , respectively. Blue values indicate a direction of $\nabla \times \mathbf{f}(\mathbf{x})$ pointing into the paper ($\mathbf{e}_r \times \mathbf{e}_\theta$) red values that one out of it ($-\mathbf{e}_r \times \mathbf{e}_\theta$). The dashed line limits the boundary layer of thickness $\delta/2$ where the electromagnetic force density and its curl decrease exponentially to $1/e$ of their values at the surface.

such that the r -dependent part of Eqs. (24) and (25) finally reads

$$\frac{R_S}{2q^2} \text{Im} \left[\tilde{\Gamma}_l^*(r) \frac{\partial}{\partial r} \tilde{\Gamma}_l(r) \right] = \text{Im} \left[\frac{\tilde{z}}{r/R_S} \frac{J_{l-1/2}(\tilde{z}r/R_S) J_{l+1/2}^*(\tilde{z}r/R_S)}{J_{l-1/2}(\tilde{z}) J_{l-1/2}^*(\tilde{z})} \right]. \tag{26}$$

4. Influence of the “skin effect”

In the experimental praxis, the ISS-EML levitation facility applies alternating magnetic fields with frequencies of $\omega/2\pi \approx 370$ kHz (heating field) and of $\omega/2\pi \approx 150$ kHz (positioning field) to liquid metal samples with radii in the range of $3 \text{ mm} \leq R_S \leq 4 \text{ mm}$ and electrical conductivities in the range of $0.5 \times 10^6 (\Omega\text{m})^{-1} \leq \sigma \leq 5 \times 10^6 (\Omega\text{m})^{-1}$. This means that the relation $q = R_S/\delta$, defined in Eq. (20), varies in the range of $2.5 < q < 11$ for the magnetic heating field and in the range of $1.5 < q < 7$ for the magnetic positioning field. This allows in consideration of (20) and with the representation of $J_{l+1/2}$ given in Ref. 22 [Eq. (8.462)] to approximate the half-integer order Bessel functions appearing in Eq. (19) by

$$J_{l+1/2}(\tilde{z}r/R_S) \approx \frac{\exp(\tilde{z}^*r/R_S)}{\sqrt{2\pi\tilde{z}r/R_S}} \tilde{\sigma}_l(\tilde{z}r/R_S), \tag{27}$$

with the complex function

$$\tilde{\sigma}_l(\tilde{z}) := \sum_{k=0}^l \frac{i^{-l+k-1} (l+k)!}{k! (l-k)! (2\tilde{z})^k} \tag{28}$$

for values $0 < r/R_S \leq 1$, which are not too far away from 1. For the radial dependence of $\mathbf{f}_l(\mathbf{x})$ and $\nabla \times \mathbf{f}_l(\mathbf{x})$ given by (26), this means that

$$\begin{aligned} & \frac{R_S}{2q^2} \text{Im} \left[\tilde{\Gamma}_l^*(r) \frac{\partial}{\partial r} \tilde{\Gamma}_l(r) \right] \\ & \approx \exp(-2q(1-r/R_S)) \text{Im} \left[\frac{\tilde{z}}{(r/R_S)^2} \frac{\tilde{\sigma}_{l-1}(\tilde{z}r/R_S) \tilde{\sigma}_l^*(\tilde{z}r/R_S)}{\tilde{\sigma}_{l-1}(\tilde{z}) \tilde{\sigma}_l^*(\tilde{z})} \right] \\ & < \exp\left(-\frac{R_S-r}{\delta/2}\right) \frac{R_S/\delta}{(r/R_S)^2}. \end{aligned} \tag{29}$$

The exponential decrease clearly reveals that the force density $\mathbf{f}(r, \theta)$ of Eq. (24) and its curl $\nabla \times \mathbf{f}(r, \theta)$ of Eq. (25) affect the liquid sample

mainly in a shell of thickness $\delta/2$ below the boundary of S (skin effect). This is visualized for the heating and positioning field and for two different values of the relation $q := R_S/\delta$ in the diagrams of Fig. 4. Bearing this behavior in mind, it is reasonable to assume that also the flow field $\mathbf{u}(r, \theta)$ and its vorticity $\nabla \times \mathbf{u}(r, \theta)$ driven according to Eq. (6) by $\nabla \times \mathbf{f}(\mathbf{x})$ scale near the boundary of S in radial direction with $\delta/2$, and furthermore, that together with $\max\|\nabla \times \mathbf{f}(\mathbf{x})\|$, also the maximum value of the flow speed $u_{\max} := \max\|\mathbf{u}(\mathbf{x})\|$ occurs on the boundary of S .

Since the Bessel functions can for $r \approx R_S$ and $q > 2.5$ very well be approximated by Eq. (27), the radial dependence of $\mathbf{f}(\mathbf{x})$ and $\nabla \times \mathbf{f}(\mathbf{x})$ given by Eq. (29) finally assumes for $r = R_S$ and $q > 2.5$ the simple expression

$$\frac{R_S}{2q^2} \text{Im} \left[\tilde{\Gamma}_l^*(r) \frac{\partial}{\partial r} \tilde{\Gamma}_l(r) \right]_{r=R_S} \approx q \text{Im} \left[(1-i) \frac{\tilde{\sigma}_l^*((1-i)q)}{\tilde{\sigma}_{l-1}^*((1-i)q)} \right] = q \left(1 - \frac{1}{q} + O(1/q^2) \right), \quad (30)$$

where the relation of the complex conjugated functions $\tilde{\sigma}_l$, defined in (28), has been expanded up to the first order in $1/q$.

D. The non-linear convection term

In spherical coordinates, $\mathbf{x} = (r, \theta, \varphi)$ with origin in the center of S and unit vectors $\mathbf{e}_r(\theta, \varphi)$, $\mathbf{e}_\theta(\theta, \varphi)$, and $\mathbf{e}_\varphi(\varphi)$ defined in Eq. (A1), cf. Fig. 3, the rotationally invariant, two-dimensional fluid flow field in the (r, θ) half-plane can be described by

$$\mathbf{u}(\mathbf{x}) = u_r(r, \theta) \mathbf{e}_r(\theta, \varphi) + u_\theta(r, \theta) \mathbf{e}_\theta(\theta, \varphi). \quad (31)$$

With this result and in consideration of Eq. (A2), the vorticity defined in Eq. (7) assumes the form

$$\begin{aligned} \Omega(\mathbf{x}) &= \frac{\mathbf{e}_\varphi(\varphi)}{r} \left(\left\{ 1 + r \frac{\partial}{\partial r} \right\} u_\theta(r, \theta) - \frac{\partial}{\partial \theta} u_r(r, \theta) \right) \\ &=: \Omega(r, \theta) \mathbf{e}_\varphi(\varphi). \end{aligned} \quad (32)$$

Accordingly, the boundary conditions (4) and (5) at the surface of the spherical sample S , that is, for points $\mathbf{x}_B = (R_S, \theta, \varphi)$ for which $\mathbf{n}(\mathbf{x}_B) = \mathbf{e}_r(\theta, \varphi)$ and $\boldsymbol{\tau}(\mathbf{x}_B) = \mathbf{e}_\theta(\theta, \varphi)$, amount to

$$u_r(R_S, \theta) = 0 \quad (33)$$

and

$$\frac{\partial}{\partial r} u_\theta(r, \theta) \Big|_{r=R_S} = \frac{u_\theta(R_S, \theta)}{R_S}, \quad (34)$$

respectively. In calculating (34), it has been considered that with (33) also $\partial u_r(R_S, \theta)/\partial \theta = 0$. With these results, the magnitude of the vorticity (32) on the boundary reads

$$\Omega(R_S, \theta) = 2 \frac{u_\theta(R_S, \theta)}{R_S}. \quad (35)$$

Since $\nabla \cdot \Omega(\mathbf{x}) = \nabla \cdot [\nabla \times \mathbf{u}(\mathbf{x})] \equiv 0$ and due to Eq. (2), the double vector product in the first the non-linear convection term of the modified Navier–Stokes equation (6) leads to

$$\begin{aligned} \nabla \times [\mathbf{u} \times \Omega] &= \nabla \cdot [\Omega \mathbf{u}] - \nabla \cdot [\mathbf{u} \Omega] = \Omega \cdot \nabla \mathbf{u} - \mathbf{u} \cdot \nabla \Omega \\ &= \mathbf{e}_\varphi \left((u_r + u_\theta \cot \theta) \frac{\Omega}{r} - u_r \frac{\partial}{\partial r} \Omega - \frac{u_\theta}{r} \frac{\partial}{\partial \theta} \Omega \right), \end{aligned} \quad (36)$$

where for its representation in spherical coordinates, Eqs. (31), (32), and (A2) have been applied. As already mentioned above, we are only interested in the value of the maximum velocity $u_{\max} := \max\|\mathbf{u}(\mathbf{x})\|$ of the flow field, which we expect to be located on the boundary of S in the point $\mathbf{x}_{\max} = (R_S, \theta_{\max})$, cf. Fig. 2. Due to (33), this means that $u_{\max} = u_\theta(R_S, \theta_{\max})$. In consideration of (33)–(35) and the property $\partial u_\theta(R_S, \theta)/\partial \theta|_{\theta=\theta_{\max}} = 0$ for a local velocity maximum on the boundary, Eq. (36) simplifies at \mathbf{x}_{\max} to

$$\nabla \times [\mathbf{u}(\mathbf{x}) \times \Omega(\mathbf{x})]_{\mathbf{x}=\mathbf{x}_{\max}} = 2 \frac{\mathbf{e}_\varphi}{R_S^2} \cot \theta_{\max} u_{\max}^2 = \mathbf{e}_\varphi \frac{u_{\max}^2}{R_S^2} A_\rho(\theta_{\max}), \quad (37)$$

where the coefficient $A_\rho(\theta_{\max})$ is a dimensionless, scalar constant representing the constant part in the second term of (37). It is worth noting, however, that $A_\rho(\theta_{\max})$ depends on the flow field $\mathbf{u}(\mathbf{x})$ at hand and may be considered to be constant only when the flow pattern and the location of \mathbf{x}_{\max} on the boundary of S do not change. For the two different flow fields, as shown in Fig. 2, which are generated by the two different force density fields $\mathbf{f}_l(\mathbf{x})$ of the ISS-EML facility, different values of $A_\rho(\theta_{\max})$ have to be expected. The same holds if the flow field changes from laminar to turbulent.

E. The shear stress term

In spherical coordinates, $\mathbf{x} = (r, \theta, \varphi)$ with origin in the center of S the radial differentiation of the mass conservation equation (2) [cf. Eq. (A2)] yields in the present two-dimensional case

$$\begin{aligned} 0 &= r^2 \frac{\partial^2}{\partial r^2} u_r(r, \theta) + 3r \frac{\partial}{\partial r} u_r(r, \theta) + r \frac{1}{\sin \theta} \frac{\partial}{\partial \theta} \left[\sin \theta \frac{\partial}{\partial r} u_\theta(r, \theta) \right] \\ &= r^2 \frac{\partial^2}{\partial r^2} u_r(r, \theta) - 6u_r(r, \theta) - \frac{1}{\sin \theta} \frac{\partial}{\partial \theta} \left[\sin \theta \left\{ 3 - r \frac{\partial}{\partial r} \right\} u_\theta(r, \theta) \right] \end{aligned} \quad (38)$$

after insertion of (2). On the surface of S , that is, for all points $\mathbf{x}_B = (R_S, \theta)$, Eq. (38) leads in consideration of (33)–(35) finally to

$$0 = R_S \frac{\partial^2}{\partial r^2} u_r(r, \theta) \Big|_{r=R_S} - \frac{1}{\sin \theta} \frac{\partial}{\partial \theta} [\Omega(R_S, \theta) \sin \theta]. \quad (39)$$

Another relation on the boundary of S results from Eq. (8). In consideration of Eqs. (24), (32)–(34), and (A2), it reads in spherical coordinates and after scalar multiplication with \mathbf{e}_φ ,

$$\begin{aligned} \rho \frac{\partial}{\partial \theta} \frac{u_\theta^2(R_S, \theta)}{2} &= \eta \frac{\partial}{\partial r} [r \Omega(r, \theta)] \Big|_{r=R_S} \\ &= \frac{\eta}{R_S} \left(R_S^2 \frac{\partial^2}{\partial r^2} u_\theta(r, \theta) \Big|_{r=R_S} + 2u_\theta(R_S, \theta) \right. \\ &\quad \left. + \frac{\partial}{\partial \theta} \frac{1}{\sin \theta} \frac{\partial}{\partial \theta} [u_\theta(R_S, \theta) \sin \theta] \right), \end{aligned} \quad (40)$$

where the last term results from the use of Eq. (2) in spherical coordinates. At the point $\mathbf{x}_{\max} = (R_S, \theta_{\max})$ on the boundary of S , where the local maximum flow velocity $u_{\max} = u_\theta(R_S, \theta_{\max})$ with the property

$\partial u_\theta(R_S, \theta)/\partial \theta|_{\theta=\theta_{\max}} = 0$ is located, Eq. (40) leads finally to the relation

$$R_S^2 \frac{\partial^2}{\partial r^2} u_\theta(r, \theta_{\max}) \Big|_{r=R_S} = \left(\frac{1}{\sin^2(\theta_{\max})} - 2 \right) u_{\max} - \frac{\partial^2}{\partial \theta^2} u_\theta(R_S, \theta) \Big|_{\theta=\theta_{\max}} = \frac{A_{\eta 1}(\theta_{\max})}{3} u_{\max}, \quad (41)$$

where the coefficient $A_{\eta 1}(\theta_{\max})/3$ is a dimensionless constant representing the constant factor in the second term of (41) as well as the parameter independent scale of the angular differentiation, see Fig. 2.

Regarding (32) the double curl operation on $\Omega(\mathbf{x})$, which appears in the second, the shear stress term of the modified Navier–Stokes equation (6) results in spherical coordinates in

$$\begin{aligned} \nabla \times [\nabla \times \Omega] &= -\frac{\mathbf{e}_\varphi}{r^3} \left(r^2 \frac{\partial^2}{\partial r^2} [r\Omega] + r \frac{\partial}{\partial \theta} \left[\frac{1}{\sin \theta} \frac{\partial}{\partial \theta} [\Omega \sin \theta] \right] \right) \\ &= -\frac{\mathbf{e}_\varphi}{r^3} \left(\left\{ 3r^2 \frac{\partial^2}{\partial r^2} + r^3 \frac{\partial^3}{\partial r^3} \right\} u_\theta - r \frac{\partial}{\partial \theta} \left[r \frac{\partial^2}{\partial r^2} u_r - \frac{1}{\sin \theta} \frac{\partial}{\partial \theta} [\Omega \sin \theta] \right] \right). \end{aligned} \quad (42)$$

In consideration of (39) and (41), Eq. (42) leads at the surface of S in the point $\mathbf{x}_{\max} = (R_S, \theta_{\max})$ finally to the simple expression

$$\nabla \times [\nabla \times \Omega(\mathbf{x})]_{\mathbf{x}=\mathbf{x}_{\max}} = -\frac{\mathbf{e}_\varphi}{R_S^3} \left(A_{\eta 1} u_{\max} + R_S^3 \frac{\partial^3}{\partial r^3} u_\theta(r, \theta_{\max}) \Big|_{r=R_S} \right). \quad (43)$$

Due to the exponential decrease in the magnetic fields inside S with increasing distance from its boundary, see Eq. (29), the local magnetic force field $\mathbf{f}(\mathbf{x})$ essentially affects the liquid sample in a shell of thickness $\delta/2$ below the boundary of S only (skin effect). Consequently, it is reasonable to assume that also the flow field $\mathbf{u}(\mathbf{x})$ scales near $r \approx R_S$ in radial direction with the conductivity σ -dependent skin depth $\delta(\sigma)$ of Eq. (20), implying that the expression $\delta^3 \cdot \partial^3 u_\theta / \partial r^3$ remains essentially constant with changing $\delta(\sigma)$. Moreover, we assume that the pattern of the flow field $\mathbf{u}(\mathbf{x})$ near $\mathbf{x}_{\max} = (R_S, \theta_{\max})$ remains nearly the same even if its magnitude $u_{\max} = \|\mathbf{u}(\mathbf{x}_{\max})\|$ changes. With these two conditions and the definitions in (20), Eq. (43) amounts to

$$\nabla \times [\nabla \times \Omega(\mathbf{x})]_{\mathbf{x}=\mathbf{x}_{\max}} = -\frac{\mathbf{e}_\varphi}{R_S^3} (A_{\eta 1} + q^3 A_{\eta 2}) u_{\max} \quad (44)$$

with dimensionless scalar constants $A_{\eta 1}(\theta_{\max})$ and $A_{\eta 2}(\theta_{\max})$ for which the same holds as for $A_\rho(\theta_{\max})$ in Sec. III D.

F. The analytical model for the maximum fluid flow velocity

Equations (25) and (30) imply that at $\mathbf{x}_{\max} = (R_S, \theta_{\max})$

$$\nabla \times \mathbf{f}_l(\mathbf{x}) \Big|_{\mathbf{x}=\mathbf{x}_{\max}} = \mathbf{e}_\varphi A_f(\theta_{\max}) \frac{\mu_0 I_0^2}{R_S^4} R_S^{2l} (q - l), \quad (45)$$

with a scalar constants $A_f(\theta_{\max})$ of dimension $[\text{m}^{-2}]$, which depends on the location of the maximum fluid velocity on the

boundary of S and thus also on the type of the magnetic field of the EML facility (heating field: $l = 1$, positioning field: $l = 2$). In Eq. (45), $I_0 := |\tilde{I}_E|$ denotes the amplitude of the alternating coil current. Insertion of the Eqs. (37), (44), and (45) in (6) results for the modified Navier–Stokes equation at $\mathbf{x}_{\max} = (R_S, \theta_{\max})$ in the simple scalar expression

$$B_2 Re^2 + (B_0 + B_1 q^3) Re - \frac{\rho}{\eta^2} \mu_0 I_0^2 R_S^{2l} (q - l) = 0, \quad (46)$$

after its scalar multiplication with \mathbf{e}_φ , after the definition of the dimensionless Reynolds number

$$Re := \frac{R_S \rho}{\eta} u_{\max}, \quad (47)$$

and after the introduction of the new composed coefficients $B_0(\theta_{\max})$, $B_1(\theta_{\max})$, and $B_2(\theta_{\max})$ of dimension (m^{2l}) . The solution of the quadratic equation (46) under consideration of the steady-state condition: $Re = 0$ if $I_0 = 0$ finally yields our physical model

$$Re = \frac{B_0 + B_1 q^3}{2B_2} \left(\sqrt{1 + \frac{4B_2}{(B_0 + B_1 q^3)^2} \frac{\rho}{\eta^2} \mu_0 I_0^2 R_S^{2l} (q - l)} - 1 \right) \quad (48)$$

for the maximum fluid flow velocity in the sample S driven by the magnetic heating field: $l = 1$ or positioning field: $l = 2$ of the ISS-EML facility.

Evidently, the Reynolds number of (47) and thus u_{\max} depends on only two parameters: $q = R_S \sqrt{\mu_0 \omega \sigma / 2}$ and $\mu_0 I_0^2 R_S^{2l} (q - l) \rho / \eta^2$, which are a combination of the known sample properties $\{R_S, \sigma, \rho, \eta\}$ and facility properties $\{\omega, I_0\}$, instead of four parameters as supposed for the surrogate model presented in Sec. II. Furthermore, there are only three *a priori* unknown coefficients $B_0(\theta_{\max})$, $B_1(\theta_{\max})$, and $B_2(\theta_{\max})$, which have to be fitted to the numerical results of the MHD calculations, instead of 21. Here, it should be reminded that the coefficients $B_n(\theta_{\max})$ depend on the pattern of the flow field at hand and may be considered to be constants only when the flow pattern near the location (R_S, θ_{\max}) of the maximum velocity does not significantly change.

IV. DETERMINATION OF THE MODEL COEFFICIENTS

A rearrangement of Eq. (46) results in

$$\underbrace{\frac{\mu_0 I_0^2 R_S^{2l} (q - l) \rho / \eta^2}{Re}}_Y = B_0 + B_1 \underbrace{q^3}_{X1} + B_2 \underbrace{Re}_{X2}. \quad (49)$$

In consideration of (20) and (47), the quantities Y, X1, and X2 defined in (49) depend on sample $\{R_S, \sigma, \rho, \eta\}$ and facility $\{\omega, I_0\}$ parameters and on the corresponding maximum fluid flow velocities u_{\max} , which have numerically been calculated for a great variety of different, physically reasonable parameter values via the MHD simulations of Ref. 18. By simple multilinear regression analysis of (49) with these data, the three coefficients B_0 , B_1 , and B_2 of the analytical model (48) could be determined. For the two flow driving force fields and the two flow models, their values are collected in Table I.

A. Heating field results

Although, as mentioned in Sec. III C 4, the EML facility processes liquid metal samples, the radii R_S and electrical resistivities σ of which

TABLE I. Coefficients of Eq. (48) for the laminar or turbulent fluid flow driven by the heating or positioning force field, respectively. Included are also the corresponding values of l and the lower limits of q , see Secs. IV A and IV B.

Force field	Flow model	l	q	B_0 (m ^{2l})	B_1 (m ^{2l})	B_2 (m ^{2l})
Heating	Laminar ($Re \lesssim 300$)	1	$\gtrsim 2.5$	7.4×10^{-3}	1.0×10^{-4}	2.9×10^{-5}
Heating	Turbulent ($Re \gtrsim 300$)	1	$\gtrsim 2.5$	3.9×10^{-3}	1.1×10^{-3}	7.7×10^{-5}
Positioning	Laminar ($Re \lesssim 300$)	2	$\gtrsim 3.5$	2.4×10^{-6}	9.6×10^{-9}	1.1×10^{-8}

result in values of $q = R_S/\delta(\sigma)$ that cover the range $1.5 < q < 11$, we have to confine for the fit of our physical model to the numerically calculated datasets of the heating field to values of

$$2.5 \lesssim q \lesssim 6. \quad (50)$$

The upper limit in (50) is due to the restricted validity of the numerical results of Ref. 18. Near the boundary of S these have been calculated on a relatively rough mesh with grid steps in radial direction on the order of $d_g \approx R_S/18$, recognizable by the distances between the flow arrows in Fig. 2. On the other hand, the typical penetration depth of the force field into the sample S is, according to Sec. III C 4, on the order of $\approx \delta(\sigma)/2$. The assumption, that reasonable results from the numerics can only be expected if the grid steps are at least a factor $\approx 2/3$ smaller than the typical variation

length of the physically relevant quantity $\delta/2$, that is, if $d_g \approx R_S/18 \lesssim (2/3)\delta/2$, led to the upper limit in (50). Note that this upper limit restricts only the validity of the numerical calculation but not that of the physical model (48).

The lower limit in (50) is due to the simplicity of the physical model (48). In order that the flow field $\mathbf{u}(\mathbf{x})$ scales near the boundary of S in radial direction with the penetration depth $\delta(\sigma)/2$, as this was supposed in Sec. III E, $\delta(\sigma)/2$ should be smaller than the typical radius of the vortex R_V , which is another length scale in the flow, c.f. Fig. 2. Driven by the heating force field, it is on the order of $R_V \approx R_S/4$ and widely constant for the different values of the sample and facility parameters.

The numerical MHD calculations of Ref. 18 for the fluid flow in S driven by the magnetic heating force field have been performed with

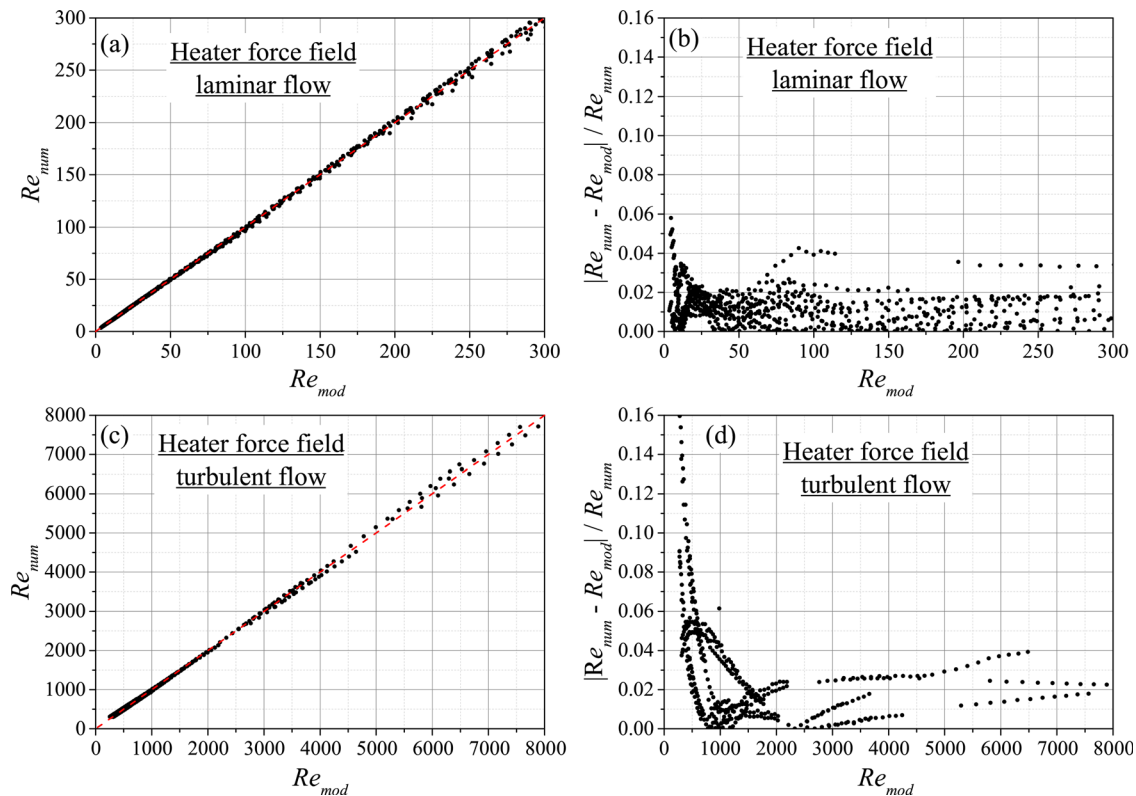


FIG. 5. Reynolds numbers in the fluid flow driven by the magnetic heating force field. The left diagrams (a) and (c) show plots of the numerically calculated Reynolds numbers: Re_{num} from the laminar and the turbulent ($k - \varepsilon$) MHD model vs the corresponding Reynolds numbers: Re_{mod} resulting from the fitted analytical model (48). The right diagrams (b) and (d) show plots of the corresponding relative deviations: $|Re_{num} - Re_{mod}|/Re_{num}$ from each other. The mean value over all data points of the latter is in both cases $< 3\%$. The turbulent model fits best for $Re \gtrsim 300$.

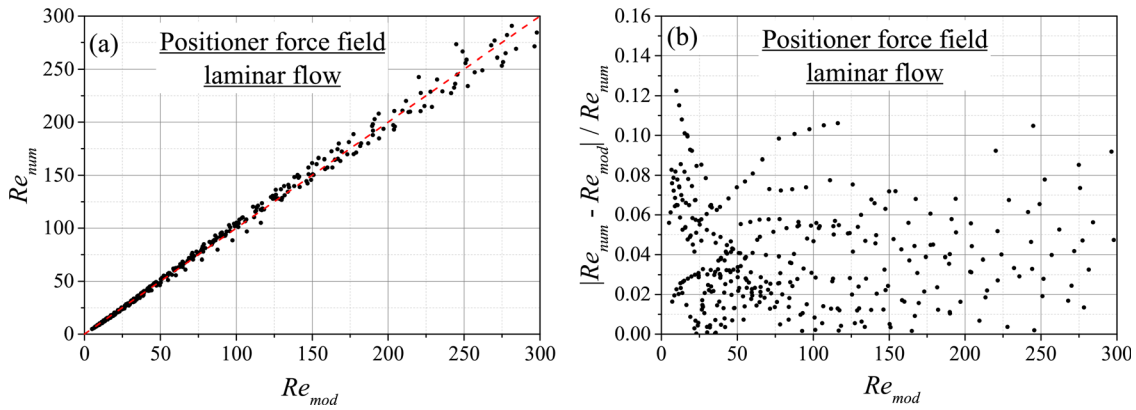


FIG. 6. Reynolds numbers in the fluid flow driven by the magnetic positioning force field. The left diagram (a) shows a plot of the numerically calculated Reynolds numbers: Re_{num} from the laminar model vs the Reynolds numbers: Re_{mod} resulting from the fitted analytical model (48). The right diagram (b) shows a plot of the corresponding relative deviations: $|Re_{num} - Re_{mod}| / Re_{num}$ from each other. The mean value over all data points of the latter is $<4\%$.

a laminar and with a turbulent (RNG $k - \epsilon$) model, respectively. The output of both calculations that also satisfies (50) consists of 1320 different datasets for $\{u_{max}, \sigma, \rho, \eta, I_0, R_S, \omega\}$ however with a sample radius and a magnetic field frequency fixed at $R_S = 3.25$ mm and $\omega/2\pi = 370$ kHz, respectively. The multilinear fit of (49) with $l = 1$ to these datasets resulted in the coefficients listed in the first two rows of Table I.

Figure 5 shows, for the whole datasets, the plots of the numerically calculated Reynolds numbers, Re_{num} , resulting from the laminar and the turbulent ($k - \epsilon$) model, respectively, vs the corresponding Reynolds numbers, Re_{mod} , resulting from the analytical model (48) with the coefficients from Table I. The diagrams demonstrate that under the conditions of Eq. (50), the numerically calculated Reynolds numbers $Re = u_{max}R_S\rho/\eta$ of the fluid flows in the liquid sample, and thus, their maximum velocities u_{max} are in the laminar and turbulent regime fairly well be reproduced by the analytical model (48).

B. Positioning field results

Driven by the positioning force field, the flow develops two toroidal vortices that compete for the place in the upper section of the liquid sphere of radius R_S , see Fig. 2(a). Compared with the situation in Sec. IV A, this results in a slightly stronger variation of the vortex extensions for different values of the sample $\{\sigma, \rho, \eta\}$ and facility $\{I_0\}$ parameters. This limits the tolerable range of $\delta(\sigma)$ from below further by a factor of ≈ 1.5 and restricts thus in the present case the range of q to

$$3.5 \lesssim q \lesssim 6. \quad (51)$$

The output of the numerical calculations of Ref. 18 for the fluid flow in S driven by the magnetic positioning force field that also satisfies (51) consists of 570 different datasets $\{u_{max}, \sigma, \rho, \eta, I_0, R_S, \omega\}$ however with a sample radius and a magnetic field frequency fixed at $R_S = 3.25$ mm and $\omega/2\pi = 150$ kHz, respectively. The multilinear fit of (49) with $l = 2$ to these datasets resulted in the coefficients listed in the last row of Table I.

Figure 6 shows for the whole datasets the plot of the numerically calculated Reynolds numbers, Re_{num} , resulting from the laminar model vs the corresponding Reynolds numbers, Re_{mod} , resulting from the

analytical model (48) with the coefficients from Table I. The diagrams demonstrate that under the conditions of Eq. (51), the numerically calculated Reynolds numbers $Re = u_{max}R_S\rho/\eta$ of the fluid flows in the liquid sample, and thus, their maximum velocities u_{max} are fairly well be reproduced by the analytical model (48).

V. SUMMARY AND PRACTICAL APPLICATIONS

The residual convective fluid flows inside liquid spherical metallic droplets processed contactlessly in the electromagnetic levitation facility ISS-EML on board the International Space Station have numerically been calculated by Xiao *et al.*^{17,18} for various values of the droplet parameters: electrical conductivity σ , mass density ρ , viscosity η , and radius R_S , and of the facility parameters: amplitude I_0 and angular frequency ω of the coil current. For an analytical representation of the maximum flow velocity u_{max} as function of these parameters, we derived the analytical model

$$Re = \frac{B_0 + B_1 q^3}{2B_2} \left(\sqrt{1 + \frac{4B_2}{(B_0 + B_1 q^3)^2} \frac{\rho}{\eta^2} \mu_0 I_0^2 R_S^2 (q - l) - 1} \right),$$

see Eq. (48), with three adjustable coefficients B_0 , B_1 , and B_2 . Here, Re denotes the Reynolds number

$$Re := \frac{R_S \rho}{\eta} u_{max},$$

see Eq. (47), and

$$q := R_S / \delta \quad \text{with} \quad \delta := \sqrt{2 / (\mu_0 \omega \sigma)}$$

TABLE II. Thermophysical properties of liquid $\text{Si}_{50}\text{Ge}_{50}$ and liquid $\text{Zr}_{64}\text{Ni}_{36}$ alloys at their respective liquidus temperatures T_{liq} . The values were taken from Refs. 14, 15, and 23.

Material	T_{liq} (K)	σ_{liq} ($\Omega^{-1} \text{ m}^{-1}$)	ρ_{liq} (kg/m^3)	η_{liq} (Pa s)
$\text{Si}_{50}\text{Ge}_{50}$	1548	1.4×10^6	5.9×10^3	$\approx 10^{-3}$
$\text{Zr}_{64}\text{Ni}_{36}$	1283	7.1×10^5	6.9×10^3	27×10^{-3}

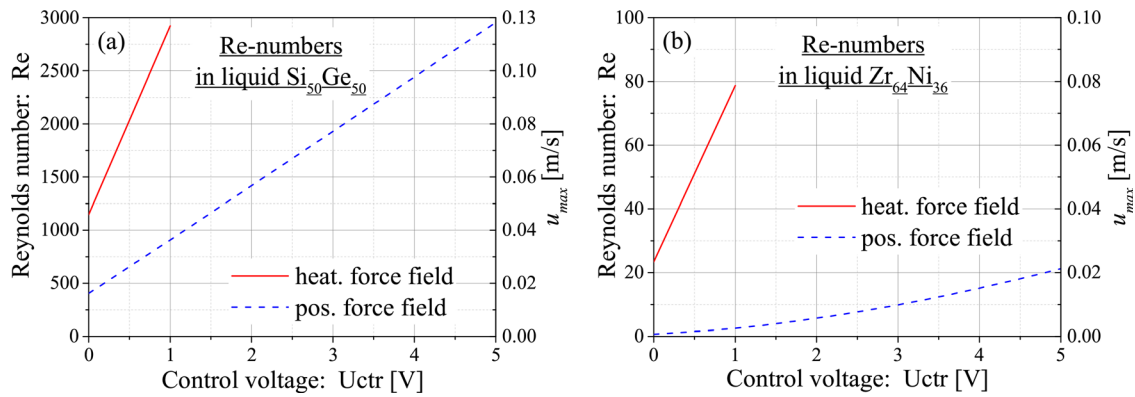


FIG. 7. Reynolds numbers: Re_{mod} and corresponding maximum flow velocities u_{max} occurring in liquid $Si_{50}Ge_{50}$ (a) and liquid $Zr_{64}Ni_{36}$ (b) droplets of $R_S = 4$ mm radius processed in the ISS-EML facility at their respective liquidus temperatures T_{liq} . Calculated with (48) the Reynolds numbers are plotted as functions of the control voltages U_{ctr} for the strength of the magnetic heating (continuous red) and positioning (dashed blue) force fields, respectively. The corresponding values of u_{max} follow from Eq. (47).

is the relation between the droplet radius R_S and the frequency ω , and conductivity σ dependent skin depth δ . Microgravity electromagnetic levitation facilities apply generally two different superposed high-frequency magnetic fields to levitated droplets: a quadrupole type positioning field and a dipole type heating field, c.f. Fig. 1. In the present investigation, we regarded them, however, separately. Typically, the local Lorentz forces caused by the dipole field generate one and those caused by the quadrupole field two toroidal vortices in the upper section of the liquid sphere, see Figs. 1 and 2. Equation (48) holds for both fields, however, with different values of the number l , coefficients B_0 , B_1 , and B_2 , and lower limits for q , which are listed in Table I.

According to the diagrams in Figs. 5 and 6, the analytical model (48) agrees together with the corresponding coefficients in Table I fairly well with the numerically calculated results.

A. Reynolds numbers in levitated $Si_{50}Ge_{50}$ and $Zr_{64}Ni_{36}$ melts

In practical applications, the strength of the high-frequency currents feed into the levitation coils by the power supplies is externally controlled by a voltage U_{ctr} . For the ISS-EML facility, the relation between these control voltages and the amplitudes of the coil current I_0 reads for the “heating current”

$$I_0^H = 24.4[A] + 22.7[A/V] U_{ctr}^H \quad (52)$$

and for the “positioning current”

$$I_0^P = 30.5[A] + 30.0[A/V] U_{ctr}^P, \quad (53)$$

where during the experimental phase the control voltages cover typically the ranges $0V \leq U_{ctr}^H \lesssim 1V$ and $0V \leq U_{ctr}^P \lesssim 5V$.

To obtain an impression on the strength of the residual fluid flows driven in liquid metallic droplets by the forces from the magnetic heating and positioning fields of the ISS-EML facility, the corresponding Reynolds numbers as function of the external control voltages have been calculated via (48) with the coefficients of Table I for a liquid $Si_{50}Ge_{50}$ and a liquid $Zr_{64}Ni_{36}$ droplet of $R_S = 4$ mm radius at its respective liquidus temperature T_{liq} .

The dedicated material parameters are listed in Table II. The results are plotted in Fig. 7.

It becomes evident from the diagrams in Fig. 7 that for both materials, the fluid flow in the droplet generated by the forces of the magnetic positioning field is much weaker than that one resulting from the heating field. Furthermore, there may occur drastic differences in the Reynolds numbers for different liquids. In the present examples, this is mainly due to the strongly different viscosities of the thin fluid $Si_{50}Ge_{50}$ melt and the highly viscous, glass-forming $Zr_{64}Ni_{36}$ melt.

The diagram of Fig. 7(a) proves that the residual fluid flows in a $Si_{50}Ge_{50}$ melt caused by the forces of the magnetic fields of the ISS-EML levitation facility are even in their idle states at $U_{ctr} = 0V$ still extremely high: $Re > 1100$. This supports the assumption in the Introduction why the viscosity measurements for the $Si_{50}Ge_{50}$ melt by means of the oscillating drop method provided physically meaningless values,¹⁵ although they have been performed in the widely forceless μg environment of the ISS.

By contrast, the diagram of Fig. 7(b), showing for $U_{ctr} = 0V$ only low Reynolds numbers ($Re \lesssim 25$), exhibits for high viscous glass-forming metallic liquids, as $Zr_{64}Ni_{36}$, residual fluid flows, which are most likely weak enough to enable in the microgravity ISS-EML levitation facility reasonable viscosity measurements via the oscillating drop method.

ACKNOWLEDGMENTS

X. Xiao acknowledges the funding support from the German Academic Exchange Service (DAAD) research fellowships.

AUTHOR DECLARATIONS

Conflict of Interest

The authors have no conflicts to disclose.

Author Contributions

Georg Lohöfer: Conceptualization (equal); Formal analysis (equal); Investigation (equal); Writing – original draft (equal); Writing – review and editing (equal). **Xiao Xiao:** Data curation (equal); Software (equal).

DATA AVAILABILITY

The data that support the findings of this study are available from the corresponding author upon reasonable request.

APPENDIX: BASIC FORMULAS IN SPHERICAL COORDINATES

For convenience, this section contains a short collection of formulas from (Ref. 24, Sec. 2.5), which are often used in the previous calculations. In a Cartesian frame of reference with the constant orthogonal unit vectors \mathbf{e}_x , \mathbf{e}_y , and \mathbf{e}_z , the orthogonal spherical unit vectors in r -, θ -, and φ -direction read

$$\begin{aligned} \mathbf{e}_r(\theta, \varphi) &= \sin \theta (\cos \varphi \mathbf{e}_x + \sin \varphi \mathbf{e}_y) + \cos \theta \mathbf{e}_z, \\ \mathbf{e}_\theta(\theta, \varphi) &= \cos \theta (\cos \varphi \mathbf{e}_x + \sin \varphi \mathbf{e}_y) - \sin \theta \mathbf{e}_z, \\ \mathbf{e}_\varphi(\varphi) &= -\sin \varphi \mathbf{e}_x + \cos \varphi \mathbf{e}_y. \end{aligned} \tag{A1}$$

The gradient, divergence, and curl operators read in spherical coordinates

$$\begin{aligned} \nabla f &= \mathbf{e}_r \frac{\partial f}{\partial r} + \frac{\mathbf{e}_\theta}{r} \frac{\partial f}{\partial \theta} + \frac{\mathbf{e}_\varphi}{r \sin \theta} \frac{\partial f}{\partial \varphi}, \\ \nabla \cdot \mathbf{v} &= \frac{1}{r^2} \frac{\partial}{\partial r} [r^2 v_r] + \frac{1}{r \sin \theta} \frac{\partial}{\partial \theta} [v_\theta \sin \theta] + \frac{1}{r \sin \theta} \frac{\partial}{\partial \varphi} v_\varphi, \\ \nabla \times \mathbf{v} &= \frac{\mathbf{e}_r}{r \sin \theta} \left(\frac{\partial}{\partial \theta} [v_\varphi \sin \theta] - \frac{\partial}{\partial \varphi} v_\theta \right) \\ &\quad + \frac{\mathbf{e}_\theta}{r} \left(\frac{1}{\sin \theta} \frac{\partial}{\partial \varphi} v_r - \frac{\partial}{\partial r} [r v_\varphi] \right), \\ &\quad + \frac{\mathbf{e}_\varphi}{r} \left(\frac{\partial}{\partial r} [r v_\theta] - \frac{\partial}{\partial \theta} v_r \right). \end{aligned} \tag{A2}$$

REFERENCES

¹E. C. Okress, D. M. Wroughton, G. Comenetz, P. H. Brace, and J. C. R. Kelly, "Electromagnetic levitation of solid and molten metals," *J. Appl. Phys.* **23**, 545–552 (1952).
²G. Lohöfer, "Theory of an electromagnetically levitated metal sphere," *SIAM J. Appl. Math.* **49**, 567–581 (1989).
³J. Brillo, G. Lohöfer, F. Schmidt-Hohagen, S. Schneider, and I. Egry, "Thermophysical property measurements of liquid metals by electromagnetic levitation," *Int. J. Mater. Prod. Technol.* **26**, 247–273 (2006).
⁴M. Mohr and H.-J. Fecht, "Investigating thermophysical properties under microgravity: A review," *Adv. Eng. Mater.* **23**, 2001223 (2021).

⁵H.-J. Fecht and R. K. Wunderlich, "Fundamentals of liquid processing in low earth orbit: From thermophysical properties to microstructure formation in metallic alloys," *JOM* **69**, 1261–1268 (2017).
⁶R. W. Hyers, "Fluid flow effects in levitated droplets," *Meas. Sci. Technol.* **16**, 394–401 (2005).
⁷J. Etay, P. Schetelat, B. Bardet, J. Priede, V. Bojarevics, and K. Pericleous, "Modelling of electromagnetic levitation: Consequence on noncontact physical properties measurements," *High Temp. Mater. Process.* **27**, 439–447 (2008).
⁸X. Xiao, J. Brillo, J. Lee, R. W. Hyers, and D. M. Matson, "Impact of convection on the damping of an oscillating droplet during viscosity measurement using the ISS-EML facility," *npj Microgravity* **7**, 36 (2021).
⁹G. P. Bracker, E. B. Baker, J. Nawer, M. E. Sellers, A. K. Gangopadhyay, K. F. Kelton, X. Xiao, J. Lee, M. Reinartz, S. Burggraf, D. M. Herlach, M. Rettenmayr, D. M. Matson, and R. W. Hyers, "The effect of flow regime on surface oscillations during electromagnetic levitation experiments," *High Temp. High Press.* **49**, 49–60 (2020).
¹⁰E. B. Baker, J. Nawer, X. Xiao, and D. M. Matson, "MHD surrogate model for convection in electromagnetically levitated molten metal droplets processed using the ISS-EML facility," *npj Microgravity* **6**, 9 (2020).
¹¹G. Lohöfer, "Viscosity measurement by the oscillating drop method: The case of strongly damped oscillations," *Int. J. Thermophys.* **41**, 30 (2020).
¹²G. Lohöfer and J. Piller, "The new ISS electromagnetic levitation facility: MSL-EML," AIAA Paper No. 2002-0764, 2002.
¹³A. Seidel, W. Soellner, and C. Stenzel, "EML—An electromagnetic levitator for the International Space Station," *J. Phys.: Conf. Ser.* **327**, 012057 (2011).
¹⁴G. Lohöfer, "High-resolution inductive measurement of electrical resistivity and density of electromagnetically levitated liquid metal droplets," *Rev. Sci. Instrum.* **89**, 124709 (2018).
¹⁵Y. Luo, B. Damaschke, G. Lohöfer, and K. Samwer, "Thermophysical properties of a Si₅₀Ge₅₀ melt measured on board the International Space Station," *npj Microgravity* **6**, 10 (2020).
¹⁶B. Li, "The fluid flow aspects of electromagnetic levitation processes," *Int. J. Eng. Sci.* **32**, 45–67 (1994).
¹⁷X. Xiao, R. W. Hyers, and D. M. Matson, "Surrogate model for convective flow inside electromagnetically levitated molten droplet using magnetohydrodynamic simulation and feature analysis," *Int. J. Heat Mass Transfer* **136**, 531–542 (2019).
¹⁸X. Xiao, J. Lee, R. W. Hyers, and D. M. Matson, "Numerical representation for flow velocity and shear rate inside electromagnetically levitated droplets in microgravity," *npj Microgravity* **5**, 7 (2019).
¹⁹G. Lohöfer, "An electrically conducting sphere in a three-dimensional, alternating magnetic field," *IMA J. Appl. Math.* **68**, 1–21 (2003).
²⁰J. D. Jackson, *Classical Electrodynamics*, 2nd ed. (Wiley, New York, 1975).
²¹M. Abramowitz and I. A. Stegun, *Pocketbook of Mathematical Functions* (Harri Deutsch, Frankfurt, 1984).
²²I. S. Gradshteyn and I. M. Ryzhik, *Table of Integrals, Series, and Products*, 5th ed. (Academic Press, San Diego, 1994).
²³P. Heintzmann, F. Yang, S. Schneider, G. Lohöfer, and A. Meyer, "Viscosity measurements of metallic melts using the oscillating drop technique," *Appl. Phys. Lett.* **108**, 241908 (2016).
²⁴G. Arfken, *Mathematical Methods for Physicists*, 3rd ed. (Academic Press, San Diego, 1985).